

Surface and vortex structures in noncentrosymmetric superconductors under applied magnetic fields

Masatosi Oka, Masanori Ichioka, and Kazushige Machida
Department of Physics, Okayama University, Okayama 700-8530, Japan
 (Dated: February 6, 2008)

We investigate how the macroscopic spatial structure of broken inversion symmetry manifests in noncentrosymmetric superconductors, by the microscopic broken inversion symmetry of the crystal structure. Based on the time-dependent Ginzburg-Landau theory including the Pauli paramagnetic effect and the Rashba interaction, we demonstrate that the centrosymmetric structures of the internal field and the screening current are broken macroscopically. The flow structure of paramagnetic supercurrent spontaneously induce the flux flow without applying external currents.

PACS numbers: 74.25.Op, 74.25.-q, 74.20.De, 74.70.Tx

I. INTRODUCTION

Recently, several heavy fermion superconductors breaking inversion symmetry in the crystal structure were successively discovered, such as CePt₃Si,¹ UIr,² and CeRhSi₃,³ and attract much attention. In the noncentrosymmetric superconductors, there appear some exotic properties through the spin-orbit coupling of the Rashba interaction which induces Fermi surface splitting between two helical spin projections.^{4,5} For the superconductivity on the Fermi surfaces, the special pairing form is only possible in the case of the spin-triplet pairing channel, or the upper critical field can exceed the Pauli-Clogston limiting field even for the spin-singlet pairing.⁶ Furthermore, application of a magnetic field makes the superconductivity more exotic, such as helically modulated superconducting order parameter,⁷ and spin polarization $\mathbf{M}_s \propto \mathbf{n} \times \mathbf{J}_s$ induced by a supercurrent \mathbf{J}_s , where \mathbf{n} is the unit vector along the polar axis of the noncentrosymmetry. Then, the paramagnetic supercurrent $\nabla \times \mathbf{M}_s$ also appears in association with \mathbf{M}_s .^{8,9,10}

The purpose of this paper is to show how the macroscopic structures of broken inversion symmetry appear in noncentrosymmetric superconductors whose microscopic inversion symmetry is broken in the crystal structure, with a view to detecting experimentally direct evidence of the noncentrosymmetric superconductors. In the presence of the time reversal symmetry at a zero field, we can not expect the broken-centrosymmetric spatial structure, since the band structure in momentum space still conserves the inversion symmetry even in the noncentrosymmetric crystal structure.¹¹ Under magnetic fields, by the combined two broken inversion symmetries of space and time, exotic noncentrosymmetric spatial structures will be revealed. We will see how these structures of the internal field and the screening current appear both in the Meissner state and in the mixed state by the paramagnetic effect, using the simulation of the time-dependent Ginzburg-Landau (TDGL) theory.

We describe the TDGL equation for the noncentrosymmetric superconductors and explain the method of our calculation in Sec. II. In Sec. III, we consider noncen-

trosymmetric spatial structures of the screening current and the penetrating internal magnetic field near surfaces in the Meissner state. In Sec. IV, we study exotic spatial structures of the current and the internal field around a vortex. These structures induce the spontaneous flux flow without applying external currents. The last section is devoted to the summary.

II. NUMERICAL SIMULATION FOR NONCENTROSYMMETRIC SUPERCONDUCTORS

Numerical simulation of the TDGL equation is one of methods to investigate dynamical and static properties of superconductivity. The theory assumes that time evolutions of an order parameter Δ and a vector potential \mathbf{A} depend on the relaxation processes of a superconducting free energy to the equilibrium. Thus, the TDGL equation is obtained by¹²

$$\frac{\partial \Delta}{\partial t} = -\frac{\delta F}{\delta \Delta^*}, \quad \frac{\partial \mathbf{A}}{\partial t} = -\frac{\delta F}{\delta \mathbf{A}}, \quad (1)$$

in an appropriate unit for times, where F is a superconducting free energy, and $\delta/\delta x$ indicates a functional derivative with respect to x .

Hamiltonian of a noncentrosymmetric s -wave superconductor with the Rashba interaction is expressed as

$$\mathcal{H} = \int d\mathbf{r} \left\{ \psi^\dagger \left(\frac{p^2}{2m} \sigma_0 + (\alpha \mathbf{p} \times \mathbf{n} + \mu_B \mathbf{B}) \cdot \boldsymbol{\sigma} \right) \psi + g \psi^\dagger i \sigma_y \psi \psi^\dagger i \sigma_y \psi \right\}, \quad (2)$$

with the electron momentum $\mathbf{p} = -i\hbar\nabla$, the spin-orbit coupling constant α , the Bohr magneton μ_B , the pairing interaction g , and the 2×2 unit matrix σ_0 , and the Pauli matrix $\boldsymbol{\sigma} = (\sigma_x, \sigma_y, \sigma_z)$. ψ is a field operator of the conduction electrons. For simplicity, we consider the case of a single component order parameter, neglecting the mixture of different parity components of the order parameter.^{6,13} We also neglect the interband pairing between split bands of $\pm \mathbf{p} \times \mathbf{n}$ spin projections, since we consider the case when the band splitting energy due to

the Rashba-interaction is enough large, as shown in the band structure calculation of CePt₃Si.¹¹

From the Hamiltonian (2), the GL free energy is obtained as^{7,14}

$$F = \int dV \left[|a| |\Psi|^2 + \frac{b}{2} |\Psi|^4 + \gamma \left| \left(-i\hbar \nabla + \frac{2\pi}{\phi_0} \mathbf{A} \right) \Psi \right|^2 + \frac{1}{8\pi} |\mathbf{B} - \mathbf{H}|^2 + \varepsilon \mathbf{n} \cdot \mathbf{B} \times \left\{ \Psi^* \left(-i\hbar \nabla + \frac{2\pi}{\phi_0} \mathbf{A} \right) \Psi + c.c. \right\} \right], \quad (3)$$

for the order parameter Ψ , where a , b , and γ are coefficients depending on the details of Fermi surface structure, ϕ_0 is the flux quantum. \mathbf{B} and \mathbf{H} are, respectively, internal and external magnetic fields. The last term with material dependent coefficient ε ($\propto \alpha \mu_B$) appears due to the absence of the inversion symmetry. The expression of Eq. (3) is also applicable to the single component case in p -wave pairing, as well as s -wave pairing. In a dimensionless form, Eq. (3) is written as

$$F = \int dV \left\{ -|\Delta|^2 + \frac{1}{2} |\Delta|^4 + \frac{1}{1-T} |(-i\nabla + \mathbf{A}) \nabla|^2 + \frac{\kappa^2}{(1-T)^2} \left(|\mathbf{B} - \mathbf{H}|^2 - \varepsilon \mathbf{n} \cdot \mathbf{B} \times \mathbf{J}_s \right) \right\}, \quad (4)$$

where Δ is the normalized order parameter, κ is the GL parameter, \mathbf{J}_s is the supercurrent density defined by

$$\mathbf{J}_s \equiv -(1-T) \text{Re} [\Delta^* (-i\nabla + \mathbf{A}) \Delta] / \kappa^2. \quad (5)$$

Here, ε is normalized by $\pi a_0 \xi_0^3 / \hbar \phi_0$, where a_0 and ξ_0 are zero temperature values of a and coherence length, respectively. Using Eqs. (1) and (4), we obtain the TDGL equation coupled with Maxwell equations

$$\frac{\partial \Delta}{\partial t} = -(1-T) (-\Delta + \Delta^2 \Delta^*) + (-i\nabla + \mathbf{A})^2 \Delta + \varepsilon (\mathbf{n} \times \mathbf{B}) \cdot (-i\nabla + \mathbf{A}) \Delta + \frac{\varepsilon}{2} \Delta (-i\nabla) \cdot (\mathbf{n} \times \mathbf{B}), \quad (6)$$

$$\frac{1}{\kappa^2} \frac{\partial \mathbf{A}}{\partial t} = -\frac{1-T}{\kappa^2} \text{Re} [\Delta^* (-i\nabla + \mathbf{A} + \varepsilon \mathbf{n} \times \mathbf{B}) \Delta] - \nabla \times (\mathbf{B} - \mathbf{M}_s), \quad (7)$$

where the spin polarization $\mathbf{M}_s \propto \mathbf{n} \times \mathbf{J}_s$ is defined as

$$\mathbf{M}_s \equiv -\varepsilon \frac{1-T}{\kappa^2} \mathbf{n} \times \text{Re} [\Delta^* (-i\nabla + \mathbf{A}) \Delta]. \quad (8)$$

In the case of uniform \mathbf{B} , we see from Eq. (6) that Δ has phase factor of the helical state as $\Delta(\mathbf{r}) = \tilde{\Delta}(\mathbf{r}) e^{-i\varepsilon(\mathbf{n} \times \mathbf{B}) \cdot \mathbf{r}}$.⁷ When this form of Δ is substituted to Eq. (7), the ε -dependence in $\Delta^* (-i\nabla + \mathbf{A} + \varepsilon \mathbf{n} \times \mathbf{B}) \Delta$ vanishes. Then, no additional diamagnetic current are induced by the phase factor of the helical state in the case of the uniform \mathbf{B} . On the contrary, $\nabla \times \mathbf{M}_s$ in Eq. (7) gives the ε -dependence due to the phase of the helical state, because $\varepsilon \mathbf{n} \times \mathbf{B}$ is absent in Eq. (8). When

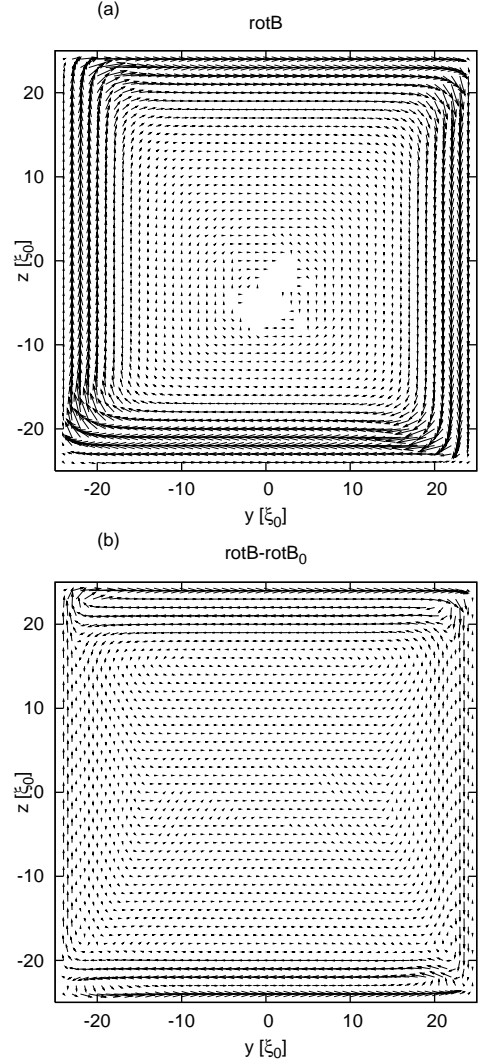


FIG. 1: Spatial distribution of the current flow in the Meissner state. We plot $\nabla \times \mathbf{B}$ in (a) and $\nabla \times \mathbf{B} - \nabla \times \mathbf{B}_0$ in (b) for the region of $50\xi_0 \times 50\xi_0$ with open boundary. The length of arrow indicates the amplitude of the current.

\mathbf{B} has spatial variation, the phase factor of the helical state becomes nontrivial, and the ε -dependence appears also from other terms in Eqs. (6)-(8). Our calculations totally include contributions from the phase factor of the helical order parameter in Eq. (6), spin polarization \mathbf{M}_s , and effects of nonuniform \mathbf{B} . These induce the noncentrosymmetric structure in the macroscopic length scale.

We perform numerical simulations following the time-evolution given by Eqs. (6)-(8), as in previous works for centrosymmetric superconductors.^{15,16,17,18} We consider the case $\mathbf{n} = (0, 0, 1)$ as in CePt₃Si and CeRhSi₃,^{19,20} and apply the magnetic field $\mathbf{H} = (H, 0, 0)$ along the x axis. The calculations are done in a two dimensional square region parallel to yz plane. The region size is $50\xi_0 \times 50\xi_0$ (i.e., $-25 \leq y/\xi_0 \leq 25$ and $-25 \leq z/\xi_0 \leq 25$). Outside of the region we set $\Delta = 0$ and $\mathbf{B} = \mathbf{H}$. In our calculation,

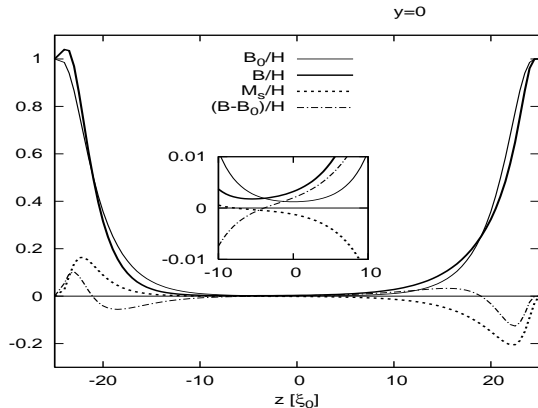


FIG. 2: Profile of the internal magnetic field in the Meissner state along a plane parallel to \mathbf{n} at $y = 0$. We plot B , B_0 , $B - B_0$ and M_s as a function of z . The inset focuses the behavior at the bulk region.

$T = 0.5T_{c,H=0,\varepsilon=0}$ and $\kappa = 2.0$, which is enough large κ to study the qualitative properties in type-II superconductors, while we use smaller κ than that of CePt_3Si for the reason of the system size and the efficiency of the simulation. We set $\varepsilon = 1$ and qualitatively study the contribution of the ε -dependent terms due to the non-centrosymmetry.

III. SURFACE STRUCTURE IN THE MEISSNER STATE

First, we discuss the screening current and the penetrating internal field near surfaces in the Meissner state, when $H = 0.04H_{c2,T=0,\varepsilon=0}$. We show the flow of the screening current $\nabla \times \mathbf{B}$ in Fig. 1 (a), and the profile of the internal field \mathbf{B} along a plane parallel to \mathbf{n} at $y = 0$ in Fig. 2. We see that, due to the screening current along the surface, B is dumped toward inside of the superconductor. We also calculate the internal field \mathbf{B}_0 when $\varepsilon = 0$ for the case of the conventional superconductor with centrosymmetry. Then, to estimate the contribution of the ε -dependent terms due to the noncentrosymmetry in GL Eqs. (6)-(8), we show the difference $\nabla \times \mathbf{B} - \nabla \times \mathbf{B}_0$ in Fig. 1(b) and $B - B_0$ in Fig. 2. From this difference, we see that spatial structure of B breaks centrosymmetry in the direction of \mathbf{n} . That is, $\mathbf{B}(\mathbf{r})$ is not symmetric for the inversion $z \leftrightarrow -z$. Qualitatively, the noncentrosymmetric structure of \mathbf{B} is due to the contribution of \mathbf{M}_s appearing near surfaces at $z = \pm 25\xi_0$. We also show M_s in Fig. 2. The contribution of ε also appears from other terms than \mathbf{M}_s , such as the phase factor of the helical state, when \mathbf{B} has spatial variation. Near the surface, \mathbf{M}_s dominantly contributes to the sign of $\mathbf{B} - \mathbf{B}_0$. Far from the surface, there appear other contributions compensating \mathbf{M}_s . As is shown in Fig. 1(b), the paramagnetic supercurrent $\nabla \times \mathbf{M}_s$ flows toward the same $+y$ -direction near both surfaces at $z = \pm 25\xi_0$. Therefore,

near the surface at $z = 25\xi_0$ ($z = -25\xi_0$), the screening current $\nabla \times \mathbf{B}$ is enhanced (suppressed) so that B is suppressed (enhanced) compared with B_0 . This indicates that the field penetration is different between $+\mathbf{n}$ and $-\mathbf{n}$ -directions.²¹

In the closed system as in our case, due to the current conservation, the backflow current to the paramagnetic current flows toward the opposite $-y$ -direction far from the surface. Therefore, contrarily to the region near the surface, the screening current $\nabla \times \mathbf{B}$ is suppressed (enhanced), so that B is enhanced (suppressed) compared with B_0 in the inside region $-4\xi_0 < z < 19\xi_0$ ($-21\xi_0 < z < -4\xi_0$).

On the other hand, in the profile of B along a plane perpendicular to \mathbf{n} at $z = 0$, $B \sim B_0$, i.e., B has symmetric profile for the inversion $y \leftrightarrow -y$.

IV. VORTEX STRUCTURE IN THE MIXED STATE

Next, we discuss the vortex structure in the mixed state, when $H = 0.15H_{c2,T=0,\varepsilon=0}$. In Fig. 3(a), we show the flow of the current $\nabla \times \mathbf{B}$, picking out $6\xi_0 \times 6\xi_0$ region around a vortex. While we set the position of the vortex center as $(y, z) = (0, 0)$ in the figure, the winding center of the current does not coincide to the vortex center, shifting to the \mathbf{n} -direction. This is due to the paramagnetic supercurrent $\nabla \times \mathbf{M}_s$. As shown in Fig. 3(b), $\nabla \times \mathbf{M}_s$ flows toward the $+y$ direction at the vortex core. And backflow of $\nabla \times \mathbf{M}_s$ returns to $-y$ -direction outside of vortex. Figure 4 shows the profile of the internal field and the current along the plane parallel to \mathbf{n} through the nearest meshpoint to the vortex center. In Fig. 4(a), we also show M_s and $B - M_s$ in addition to B . The diamagnetic component $B - M_s$ is almost symmetric for $z \leftrightarrow -z$, as in the conventional centrosymmetric superconductors. The peak position of $B - M_s$ coincides to the vortex center. However, M_s shows almost antisymmetric structure for $z \leftrightarrow -z$, since \mathbf{J}_s of $\mathbf{M}_s \propto \mathbf{n} \times \mathbf{J}_s$ changes the flow direction at $z \sim 0$. Summing up $B - M_s$ and M_s , we understand that B has noncentrosymmetric structure at the vortex.

In Fig. 4(b), we plot the y -component of the current $(\nabla \times \mathbf{B})_y$ with $(\nabla \times \mathbf{M}_s)_y$ and $(\nabla \times \mathbf{B})_y - (\nabla \times \mathbf{M}_s)_y$. The flow of the diamagnetic current component $(\nabla \times \mathbf{B})_y - (\nabla \times \mathbf{M}_s)_y$ is winding around the vortex center. The slope of M_s in Fig. 4(a) gives the paramagnetic current component $(\nabla \times \mathbf{M}_s)_y$. Since M_s is increasing near $z = 0$ in Fig. 4(a), $(\nabla \times \mathbf{M}_s)_y$ flows $+y$ direction at the vortex core. Therefore, the position where $(\nabla \times \mathbf{B})_y = 0$ deviates from $z = 0$ to $+z$ -direction. The noncentrosymmetric vortex structure, breaking cylindrical symmetry, appears due to the antisymmetric spatial structure of the spin polarization \mathbf{M}_s .

On the other hand, in the profile along a plane perpendicular to \mathbf{n} through the nearest meshpoint to the vortex center, $M_s \sim 0$ and $(\nabla \times \mathbf{M}_s)_z \sim 0$, so that B is sym-

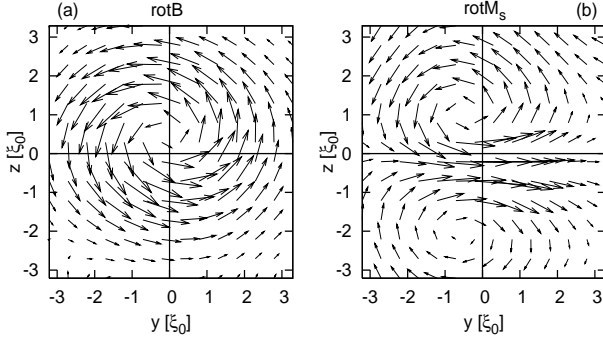


FIG. 3: Spatial distribution of the current flow around a vortex. We plot $\nabla \times \mathbf{B}$ in (a) and $\nabla \times \mathbf{M}_s$ in (b) for a focused region of $6\xi_0 \times 6\xi_0$. The length of arrow indicates the amplitude of the current. The vortex center is located at $(y, z) = (0, 0)$.

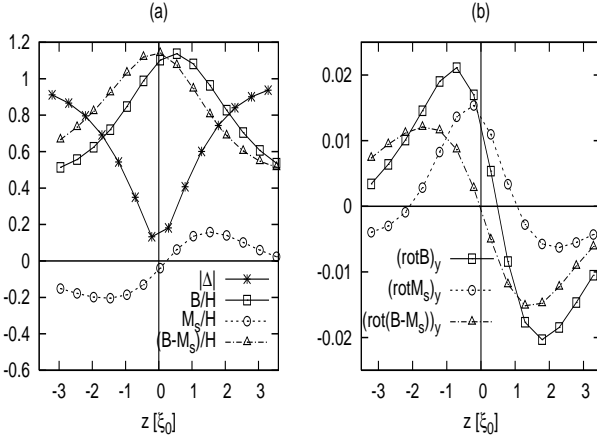


FIG. 4: Profile of the internal magnetic field (a) and the current (b) around a vortex along the plane parallel to \mathbf{n} through the nearest meshpoint to the vortex center. We plot B , M_s , $B - M_s$ and $|\Delta|$ in (a) and $(\nabla \times \mathbf{B})_y$, $(\nabla \times \mathbf{M}_s)_y$, $(\nabla \times \mathbf{B})_y - (\nabla \times \mathbf{M}_s)_y$ in (b).

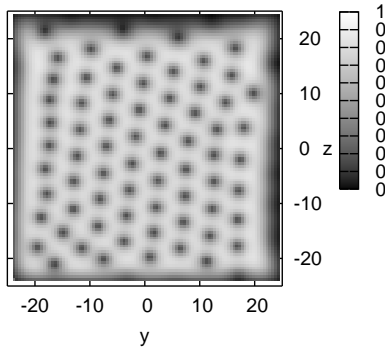


FIG. 5: Snapshot for the spatial structure of $|\Delta(\mathbf{r})|$ in the mixed state without applying external currents.²²

metric and $(\nabla \times \mathbf{B})_z$ is antisymmetric at $z = 0$ for the inversion $y \leftrightarrow -y$, as in the centrosymmetric superconductors.

The flow structure of the paramagnetic supercurrent at the vortex gives similar effects as in the situation when an external current is applied toward $+y$ direction. Then, in our simulation, the paramagnetic supercurrent spontaneously induces the flux flow even in the absence of the external current. Figure 5 shows the snapshot of the spatial structure of $|\Delta(\mathbf{r})|$ when $H = 0.3H_{c2, T=0, \varepsilon=0}$.²² In this simulation without applying external currents, new vortices are generated in the upper (positive z) surface continuously, and finally they move out to the lower (negative z) surface after moving to lower side. The vortices do not form stationary lattice permanently. In our simulation, the local voltage ($\propto \partial \mathbf{A} / \partial t$)¹⁷ appears in the vortex.

The above-mentioned broken-centrosymmetric features of the noncentrosymmetric superconductors appear, when the magnetic field \mathbf{H} is applied perpendicular to \mathbf{n} . In the study of the vortex structure when \mathbf{H} is parallel to \mathbf{n} ,^{7,23} the spin polarization \mathbf{M}_s appears toward the radial direction around a vortex, and the vortex structure remains to be cylindrical symmetric.

V. SUMMARY

We have shown how broken-centrosymmetric spatial structures appear in the macroscopic scale of the noncentrosymmetric superconductors. We investigate the surface structure in the Meissner state and the vortex structure in the mixed state, by numerical simulations of the TDGL equation. When an applied field \mathbf{H} is perpendicular to \mathbf{n} , the broken-centrosymmetric spatial structures of the internal magnetic field and the screening current are induced by the characteristic paramagnetic effect due to the Rashba interaction. Namely, the field penetration in the Meissner state becomes anisotropic between $+\mathbf{n}$ and $-\mathbf{n}$ -directions. And the antisymmetric spin polarization \mathbf{M}_s around a vortex breaks cylindrical symmetry of the vortex. The paramagnetic supercurrent at a vortex center given by the antisymmetric \mathbf{M}_s may induce the flux flow without applying external currents. We hope that these phenomena will be observed in future experiments, as direct evidence of the noncentrosymmetric superconductors.

ACKNOWLEDGEMENT

We thank Hiroto Adachi for useful discussions.

-
- ¹ E. Bauer, G. Hilscher, H. Michor, Ch. Paul, E.W. Scheidt, A. Gribanov, Yu. Seropegin, H. Noel, M. Sigrist, and P. Rogl, Phys. Rev. Lett. **92**, 027003 (2004).
 - ² T. Akazawa, H. Hidaka, T. Fujiwara, T. C. Kobayashi, E. Yamamoto, Y. Haga, R. Settai, Y. Ōnuki, J. Phys.: Condens Matter **16**, L29 (2004).
 - ³ N. Kimura, K. Ito, K. Saitoh, Y. Umeda, H. Aoki, and T. Terashima Phys. Rev. Lett. **95**, 247004 (2005).
 - ⁴ E.I. Rashba, Sov. Phys. Solid State **2**, 1109 (1960).
 - ⁵ Fermi surface splitting due to the absence of inversion symmetry is recently observed experimentally in a surface of Sb(111); K. Sugawara, T. Sato, S. Souma, T. Takahashi, M. Arai, and T. Sasaki, Phys. Rev. Lett. **96**, 046411 (2006).
 - ⁶ P.A. Frigeri, D.F. Agterberg, A. Koga, and M. Sigrist, Phys. Rev. Lett. **92**, 097001 (2004).
 - ⁷ R.P. Kaur, D.F. Agterberg, and M. Sigrist, Phys. Rev. Lett. **94**, 137002 (2005).
 - ⁸ V.M. Edelstein, Phys. Rev. Lett. **75**, 2004 (1995).
 - ⁹ S.K. Yip, Phys. Rev. B **65**, 144508 (2002).
 - ¹⁰ S. Fujimoto, Phys. Rev. B **72**, 024515 (2005).
 - ¹¹ K.V. Samokhin, E.S. Zijlstra, and S.K. Bose, Phys. Rev. B **69**, 094514 (2004).
 - ¹² L.P. Gor'kov and G.M. Eliashberg, Zh. Eksp. Teor. Fiz. **54**, 612 (1968) [Sov. Phys. JETP **27**, 328 (1968)].
 - ¹³ L.P. Gor'kov and E.I. Rashba, Phys. Rev. Lett. **87**, 037004 (2001).
 - ¹⁴ V.M. Edelstein, J. Phys.: Condens. Matter **8**, 339 (1996).
 - ¹⁵ R. Kato, Y. Enomoto, and S. Maekawa, Physica C **227**, 387 (1994).
 - ¹⁶ R. Kato, Y. Enomoto, and S. Maekawa, Phys. Rev. B **47**, 8016 (1993).
 - ¹⁷ M. Machida and H. Kaburaki, Phys. Rev. Lett. **71**, 3206 (1993).
 - ¹⁸ Y. Matsunaga, M. Ichioka, and K. Machida, Phys. Rev. Lett. **92**, 157001 (2004) ; Phys. Rev. B **70**, 100502(R) (2004).
 - ¹⁹ E. Yamamoto, Y. Haga, T.D. Matsuda, A. Nakamura, R. Settai, Y. Inada, H. Sugawara, H. Sato, and Y. Ōnuki, J. Nucl. Sci. Technol. **3**, (Suppl.) 187 (2002).
 - ²⁰ P.A. Frigeri, D.F. Agterberg, A. Koga and M. Sigrist, Physica B **359-361**, 371 (2005).
 - ²¹ S.K. Yip, J. Low Temp. Phys. **140**, 67 (2005).
 - ²² See EPAP Document No. [number will be inserted by publisher] for movie version of Fig. 5.
 - ²³ N. Hayashi, Y. Kato, P.A. Frigeri, K. Wakabayashi, and M. Sigrist, cond-mat/0510548.